Supporting Information

Reinhart et al. 10.1073/pnas.1504196112

SI Materials and Methods

Subjects. Individuals who met the *Diagnostic and Statistical Manual of Mental Disorders*, *4th Edition* (DSM-IV) criteria for schizophrenia were recruited from outpatient psychiatric facilities in Nashville, Tennessee. Diagnoses were confirmed with structured clinical interviews (Structured Clinical Interview for the DSM-IV Axis I Disorders) (1). Clinical symptoms were assessed with the Brief Psychiatric Rating Scale (2), the Scale for the Assessment of Positive Symptoms (3), and the Scale for the Assessment of Negative Symptoms (4). All patients were medicated with atypical antipsychotic drugs. The mean chlorpromazine dose equivalent was 425.05 mg·d^{-1} (SD = 250.73). All subjects were screened to exclude substance use within the past 6 mo, history of neurological disorders, history of head injury, inability to fixate, and excessive sleepiness. All subjects had normal color vision, and normal or corrected-to-normal visual acuity. All subjects gave written informed consent approved by the Vanderbilt University Institutional Review Board and were paid.

Data were collected from 19 patients with schizophrenia (17 patients completed both anodal and sham sessions, 1 patient completed only the anodal session, and 1 patient completed only the sham session) and 18 demographically matched healthy subjects (all 18 healthy subjects completed both anodal and sham sessions). The same patterns of effects were observed across all dependent variables when these analyses were restricted to the 17 patients and 18 control subjects who participated in both sessions. Subjects in each group were matched on age, gender, and handedness (Table S1). Data from three healthy subjects in the present study contributed to the grand average event-related potentials (ERPs) of 20 healthy subjects reported previously (5). These individuals demographically matched three individuals from our sample of patients with schizophrenia.

Stimuli and Procedures. Each subject received anodal and sham tDCS on different days. Order of the anodal and sham sessions was randomized across subjects. Immediately following stimulation, subjects performed a color discrimination task (i.e., a modified go/no-go task) (Fig. 1*A*), while we recorded their EEG oscillations.

All trials began with central fixation (0.37° square, 30 cd/m^2, 800–1200 ms), followed by a peripheral target (1° × 1°, 10° from the center of screen along the horizontal meridian, 700 ms) that appeared to the left of fixation in half of the trials and to the right in the remainder of the randomly interleaved trials [i.e., no-stop trials (66% of all trials)]. To ensure that subjects committed a sufficient number of errors, a stop signal appeared (a central square subtending 0.66°, with 0.08° line width, 30 cd/m^2) on a randomly interleaved subset of trials [i.e., stop trials (33% of all trials)]. This stop signal informed subjects to withhold their response on that trial. Six stop signal delays (SSDs, the stimulus-onset asynchrony between on the onset of the target and the onset of the stop signal) were sampled with equal probability: 60, 120, 180, 240, 300, and 360 ms, because this SSD range has been shown to produce stop-signal success rates near 50% across all delays (6, 7). After presentation of the stop signal, stimuli remained on the screen until 700 ms had elapsed from target onset. The intertrial interval was 1,000–1,200 ms, randomly jittered with a rectangular distribution. The task duration was ~1 h.

On any given testing day, target stimuli could appear in one of three pairs of colors [red ($x = 0.612, y = 0.333, 15.1$ cd/m^2) and blue ($x = 0.146, y = 0.720, 6.41$ cd/m^2), magenta ($x = 0.295, y = 0.153, 19.3$ cd/m^2) and green ($x = 0.281, y = 0.593, 45.3$ cd/m^2), or purple ($x = 0.245, y = 0.126, 9.3$ cd/m^2) and yellow ($x = 0.408, y = 0.505, 54.1$ cd/m^2). Subjects were required to press one of two buttons on the handheld gamepad to respond to each target color. The target colors changed across days. Feedback about the accuracy of each response was provided at the end of every trial. Feedback occurred 1,000 ms after the 700-ms response window had lapsed. Feedback was in the form of a centrally presented outline of a circle (0.88° diameter, 0.13° thick) or cross (0.88° length, 0.13° thick) presented for 1,000 ms. The meaning of these symbols (i.e., correct vs. incorrect) was randomized across sessions and subjects. A 700-ms deadline for any response was imposed to ensure enough errors were made to measure brain activity and behavior reliably on error and error-following trials. Conservatively, we have cut the first 50 trials from each subject's data to remove data that may have been contaminated by learning effects during the early part of each session. Here, we focus on the neural and behavioral signatures of adaptive control during the primary course of the experiment in which the stimulus–response mapping was known and subjects were in a stable state of information processing, as much as possible.

The tDCS was administered using a battery-driven, constant-current stimulator (Mind Alive, Inc.) and pair of conductive rubber electrodes (active: 19.25 cm^2, reference: 52 cm^2). The electrodes were placed in saline-soaked synthetic sponges and held in place by a headband. The cathodal electrode was placed on the center of the right cheek to avoid confounding effects from other brain regions (5). Specifically, the cheek electrode was placed diagonally, 3 cm from the cheilion (lip corner at rest) along an imaginary line connecting the cheilion to the ipsilateral condylion (palpable when the jaw is moved) (Fig. 1*E*). The anodal electrode was place over medial-frontal cortex (site FCz, from the International 10–20 System), and current was applied for 20 min at an intensity of 1.5 mA. During stimulation, subjects were seated in a quiet room with their eyes open, not engaged in any explicit motor or cognitive task. Comparable stimulation protocols have been shown to create an excitatory (anodal) effect for up to 5 h (5). The time interval between testing days was greater than 48 h to avoid ordering confounds related to repeated brain stimulation exposure (8). The sham tDCS condition followed the same procedure, but stimulation only lasted 30 s, ramping up and down at the beginning, middle, and end of the 20-min period, simulating the periodic tingling sensation that subjects reported on active testing days. No subject reported adverse effects of stimulation beyond mild tingling or itching under the tDCS electrodes.

We took several measures to ensure that information about the experiment did not lead to biasing of the results. First, all behavioral and electrophysiological testing was conducted in a sound-attenuated, electrically shielded booth to eliminate subject–experimenter interaction, in addition to minimizing sources of electrical noise. Second, the experimenter conducting the tDCS session was different from the experimenter collecting the behavioral and electrophysiological data in all but six instances across the 72 recording sessions. Third, subjects were blinded to the presence of the stimulation. Blinding was confirmed through a series of debriefing questions. Specifically, after each testing day, we administered a safety questionnaire (9) and visual analog scale (10), which included questions regarding attention, concentration, mood, vision, headache, fatigue, and skin sensations under the tDCS electrodes. The scores from these ratings did not significantly differ by stimulation conditions for patients (each $t < 0.814, P > 0.426$) or controls (each $t < 1.112, P > 0.280$).

In addition, all subjects were pointedly asked whether they could guess which testing day they had received active stimulation. Overall, both subject groups were equally below the chance level of detecting stimulation (i.e., 50%) (controls: hit rate = 33.3%, false alarm rate = 66.7%; patients: hit rate = 31.6%, false alarm rate = 68.4%).

The raw EEG was recorded (250-Hz sampling rate, 0.01- to 100-Hz bandpass filter) with an SA Instrumentation Amplifier using nonpolarizable tin electrodes embedded in an elastic cap (Electrocap International). The electrodes were arrayed according to the International 10–20 System (Fz, Cz, Pz, F3/F4, C3/C4, P3/P4, PO3/PO4, T3/T4, T5/T6, O1/O2), including two nonstandard sites (OL, midway between O1 and T5; OR, midway between O2 and T6). Signals were referenced online to the right mastoid electrode and referenced again offline to the average of the left and right mastoids (11). Horizontal eye position was monitored by recording an electrooculogram from bipolar electrodes placed at the outer canthi of each eye. Vertical eye position and blinks were monitored with bipolar electrodes placed above and below the left orbit. Periorbital electrodes detected eye movements, and a two-step ocular artifact rejection method was used (12).

Data Analysis.

Preprocessing. Posterror slowing calculations accounted for the effects of nonstationarity on RT estimates (13). For this correction, posterror slowing was calculated as the RT on correct no-stop trial $n + 1$ minus RT on correct no-stop trial $n - 1$, where n is an error trial. All subjects had data from at least 25 error trials and at least 20 trials for single-trial analyses.

All EEG data were segmented from −1,000 to 2,000 ms periresponse, with large windows to eliminate edge artifacts induced by wavelet convolution from the critical middle of this window. All EEG segments were converted to current source density (CSD) using methods of Kayser and Tenke (14). CSD acts as a spatial high-pass filter, increasing spatial specificity and minimizing volume conduction (15). In addition, CSD has been shown to characterize local activities more accurately during the calculation of long-distance coherence (16, 17). Of note, similar tDCS-induced results were obtained when we analyzed our data using raw EEG voltages instead of the CSD-transformed data. This similarity across raw voltages and CSD transforms was true for patients with schizophrenia (intertrial phase coherence: $F_{1,17} = 5.643$, $P = 0.028$; intersite phase synchrony: Cz-F3: $F_{1,17} = 4.431$, $P = 0.049$; Cz-F4: $F_{1,17} = 5.242$, $P = 0.034$) and healthy control subjects (intertrial phase coherence: $F_{1,17} = 6.062$, $P = 0.024$; intersite phase synchrony: Cz-F3: $F_{1,17} = 7.522$, $P = 0.013$; Cz-F4, $F_{1,17} = 8.074$, $P = 0.010$).

Time-frequency analysis. Time-frequency analyses were implemented using custom MATLAB (MathWorks) routines and custom routines from FieldTrip (18). Total power and intertrial phase coherence were calculated by convolving the CSD EEG time series in each segment with a set of complex Morlet wavelets, defined with a Gaussian envelope using a constant ratio ($\sigma_f = \frac{f}{7}$) and a wavelet duration ($6\sigma_t$), where f is the center frequency and $\sigma_t = \frac{1}{2\pi\sigma_f}$. Frequencies ranged from 1 to 30 in 1-Hz steps. Following single-trial EEG spectral decomposition, we divided each complex data point by its corresponding magnitude, generating a new series of complex data where the phase angles are preserved but the magnitudes are unit-normalized. These magnitude-normalized complex values were then averaged, yielding a measure of intertrial phase coherence for each frequency, time point, and electrode. This measure varies from 0 (no phase coherence across trials) to 1 (identical phase angles across trials). In addition, the magnitude lengths of the complex number vectors were extracted, squared, and averaged, yielding a measure of cross-trial total power for a given frequency, time point, and electrode. Evoked power was calculated by performing the same procedure (i.e., squaring the magnitude values for each time and frequency

point in the time-frequency matrix) on the magnitude length of the complex number vectors, but only after critically isolating the cross-trial phase-synchronized EEG oscillations through time-domain averaging. Each segment was then cut −200 to 500 ms periresponse. Power was decibel-normalized, where for each electrode and frequency, the average power during an interval of −400 to −100 ms before target onset served as baseline activity. In sum, within-electrode intertrial phase coherence reflects the extent to which the phase angles of oscillations are consistent over trials at a single electrode at a specific point in time-frequency space, whereas power reflects the intensity of this signal.

Next, we calculated intersite phase synchrony, a measure of the consistency of phase angles between two electrodes averaged over trials. Intersite phase synchrony is defined as

$$\left| \frac{1}{n} * \sum_{t=1}^{n} e^{i[\phi_{jt} - \phi_{kt}]} \right|,$$

where n is the number of trials, and ϕ_j and ϕ_k are the phase angles of electrodes j and k, respectively.

Intersite phase synchrony varies between 0 (absence of phase synchrony) and 1 (perfect phase alignment between electrodes) for each frequency and time point. For single-trial analyses, intersite phase synchrony was calculated at each trial over time points. Intersite phase synchrony is similar to phase-locking value (19).

It is noteworthy to point out the steps we took to increase the spatial resolution of our electrophysiological measures and reduce the influence of electrical field spread. Both the Laplacian transformation and our metric of phase synchrony (unweighted by magnitude information) have been shown to diminish the effects of volume conduction and provide greater spatial precision (15–17, 19).

Current-flow model. To increase our precision in reasoning about the effects of tDCS in the brain, we computed a computational forward model of tDCS current flow. Our model of tDCS current flow was informed by previous methods (20). This process involved (*i*) MRI segmentation, (*ii*) electrode placement, (*iii*) generation of a finite element model, and (*iv*) computation. We used the MNI T1-weighted MRI reference brain from CURRY 6.0 multimodal neuroimaging software (Compumedics Neuroscan). A combination of automated and manual segmentation tools was used to obtain tissue masks, including Gaussian filters, and morphological and Boolean operations were implemented in MATLAB. Unlike previous models using simple geometries (e.g., spheres), we used realistic volumetric head geometries with a numerical solver finite element method, because this procedure should better capture realistic sulci and gyri anatomy of the cortical surface, improving the precision of our tDCS model. Volumetric mesh was generated from the segmented data (>140,000 vertices, >800,000 tetrahedral elements). Segmented compartments and their respective isotropic electrical conductivities (in siemens per meter) included skin (0.33), skull (0.0042), and brain (0.33). In short, the production of meshes is a process where each mask is divided into small contiguous elements, which then allow the current flow to be numerically computed.

Our forward computation using a finite element model was implemented in SCIRun (available as open-source software at software.sci.utah.edu). We simulated current flow with a bipolar electrode configuration, including the anode (19.25 cm²) centered over FCz and the cathode (52 cm²) centered over the right cheek between the zygomaticus major and the condylion. Current density corresponding to 1.5 mA of total current was applied at the anodal electrode, and ground was applied at the cathodal electrode.

To determine the distribution of electrical potential inside the human tissues, the Laplace equation

$$\vec{\nabla} \cdot (\sigma \vec{\nabla} \varphi) = 0,$$

(φ, potential; σ, conductivity) was solved and the following boundary conditions were used. Inward current flow = J_n (normal current density) was applied to the exposed surface of the anode. The ground was applied to the exposed surface of the cathode. All other external surfaces were treated as insulated. Plots show the cortical current density distribution. It is important to emphasize that our tDCS model serves only as a working hypothesis for where the trajectory of the electrical field passes through the brain, given our specific tDCS configuration.

Source-reconstruction model. Source estimation was performed using CURRY 6. The interpolated boundary element method model (21) was derived from averaged MNI MRI data. It consisted of 9,300 triangular meshes overall, or 4,656 nodes, which describe the smoothed inner skull (2,286 nodes), the outer skull (1,305 nodes), and the outside of the skin (1,065 nodes). The mean triangle edge lengths (node distances) were 9 mm (skin), 6.8 mm (skull), and 5.1 mm (brain compartment). Standard conductivity values for the three compartments were set as follows: skin = 0.33 S/m, skull = 0.0042 S/m, and brain = 0.33 S/m. The standardized low-resolution electromagnetic tomography (sLORETA)-weighted accurate minimum norm method (SWARM) was estimated using sensor positions based on the International 10–20 System and projected onto the T1-weighted MRI of the CURRY 6 individual reference brain. SWARM uses the methods of diagonally weighted minimum norm least squares (22) and sLORETA (23) to compute a current density vector field (24). SWARM has been shown to estimate neural source points with relatively low error for EEG dipole simulations at different cortical depths. Although source-reconstruction methods offer a reasonable estimate of the actual pattern of activity generating scalp electrode level oscillatory signals, such modeling carries with it several ambiguities. Thus, source estimates are not intended as strong claims about the location of neuronal generation but, instead, provide potential candidates with which to relate to neuroimaging and single-unit techniques.

Electrodes, frequency band, and time windows of interest. The parameters in our analyses were chosen a priori based on previously established methods. The theta band was defined from 4–8 Hz, and the Cz electrode was chosen for measuring theta oscillations from medial-frontal cortex based on prior work (25). The Cz-F3 and Cz-F4 electrode pairs were used to measure intersite phase synchrony between the medial-frontal and lateral-prefrontal regions of the head, consistent with prior work (16). We used a conservative measurement window (i.e., broad), with a periresponse from −50 to 300 ms, to quantify the theta-band activities for within- and between-electrode analyses, consistent with prior work (16, 17), with the exception of the evoked power analysis, for which the analytic window was 0–100 ms postresponse.

ERP analysis. For the error-related negativity (ERN) analysis, the continuous EEG recording was time-locked to the button-press onset and baseline-corrected to the interval from 200 to 50 ms before response (26). Stop trials on which subjects responded before stop signals were presented were not included in ERN analyses because subjects did not have the necessary information to deduce that an error had been committed. The ERN amplitude was measured from Cz using a time window from −50 to 150 ms relative to the response onset. We calculated amplitude of the voltages as the mean area under the curve of the difference wave subtracting error from correct trials (26).

Statistical Analysis. We used separate repeated measures ANOVAs for comparisons within (i.e., error vs. correct) and between stimulation condition (anodal vs. sham) and subject group (patients vs. controls) for each dependent measure. Where appropriate, follow-up

ANOVAs were conducted to test specific preplanned hypotheses. For single-trial analyses, individualized standardized β-weights were taken from bivariate regressions between a priori determined measures of adaptive-control activities (intersite phase synchrony and intertrial phase coherence) and posterror RT using the −50 to 300-ms periresponse measurement window. We adjusted P values using the Greenhouse–Geisser epsilon correction for nonsphericity when the sphericity assumption was violated (27).

For group-level statistics, we complemented our hypothesis-driven approach (described above) with a data-driven analysis using a nonparametric permutation test (28, 29) to characterize the spatiospectral specificity of the error-related EEG phase synchronization and power effects. We used a clustering algorithm that corrects for multiple comparisons. Specifically, for each electrode and frequency bin, we calculated two t values by comparing the observed value with a null distribution obtained at that electrode-frequency bin. We obtained 2% of the largest values by permuting the single subjects' observations where they exceeded the positive t value, and we obtained 2% of the smallest values by permuting the single subjects' observations where they were smaller than the negative t value. We thresholded the observed and permuted data at these t values. We defined a spatiospectral cluster as consisting of threshold-exceeding electrode-frequency points neighboring in frequency space and in physical space. For each cluster, we calculated the sum of the t statistics as the t-sum test statistic. Monte Carlo randomization was used for generating a null distribution of the maximum t-sum test statistic by randomly permuting the data between conditions for each subject (1,000 random sets of permutations were used). A significant P value was estimated based on the proportion of the randomization null distribution exceeding the observed maximum t-sum test statistics.

SI Results

In the present study, error-related EEG analyses were performed in the time-frequency domain; however, here, we report complimentary results from analyses conducted in the time-voltage domain (i.e., analyses of ERPs). Specifically, we examined the ERN, a well-established component of the human ERPs elicited by incorrect responses, which is believed to derive from neural circuits in medial-frontal cortex (26). The reader should note that we were unable to measure the feedback-related negativity (FRN) reliably due to eye movement activity that coincided with the feedback stimuli, particularly in the patient group. However, the FRN is not as heavily studied in patients with schizophrenia, unlike the ERN, which is one of the most reliably documented electrophysiological abnormalities in schizophrenia (26), consistent with work showing abnormal neural network structure, connections, and activity in the medial-frontal cortex of these patients (30, 31).

We found that delivering inward current over medial-frontal cortex increased the amplitude of the ERN in patients with schizophrenia. In the sham condition shown in Fig. S1, the ERN for patients was absent (error vs. correct waveforms: $F_{1,17} = 1.054$, $P = 0.319$), and it was significantly reduced relative to the ERN in healthy controls ($F_{1,17} = 19.948$, $P = 0.0003$), consistent with the results we observed in the components of the error-related EEG oscillations (i.e., intertrial phase coherence, total power, and evoked power) (Fig. 1D). However, after 20 min of anodal stimulation, the ERN component was apparent in patients' response-locked ERPs (Fig. S1), paralleling the selective enhancement we found in EEG phase structure (i.e., the intertrial phase coherence) (Fig. 1F).

The effect on the ERN was statistically evidenced by a significant difference in the negative potential elicited on errors vs. correct trials in the anodal condition ($F_{1,17} = 9.215$, $P = 0.007$) and a significant increase in ERN amplitude between stimulation

conditions in the same patients ($F_{1,17} = 8.892$, $P = 0.008$). Interestingly, a comparison across subject groups showed no difference between the schizophrenia ERN after anodal stimulation and the healthy control ERN after sham stimulation ($F_{1,17} = 0.972$, $P = 0.338$), again similar to our results of intertrial phase coherence. Thus, anodal stimulation to medial-frontal cortex boosted the abnormally weak error-related electrophysiological activity in patients with schizophrenia, such that the magnitude of this index of neural processes related to executive control in schizophrenia was quantitatively indistinguishable from the magnitude of this index of neural processes related to executive control in healthy subjects.

Our observation of both ERN and EEG phase coherence modulations following brain stimulation allows us to weigh in on the long-standing debate between the classical vs. synchronized oscillation theories of ERP generation. According to the classical view, ongoing EEG oscillations are treated as noise that obscures the ERP component and approaches zero by averaging across an increasing number of trials, and ERP signals are treated as being generated independent of the ongoing EEG oscillations that are averaged out (32–35). In contrast, the synchronized oscillation perspective argues that ERPs are produced when the triggering event causes a phase resetting of the ongoing EEG oscillations (36–38). Our results appear to favor theories of the latter sort, proposing that ERN generation results from at least a partial reorganization of ongoing oscillatory neural activity (39, 40), consistent with the idea that ERPs more generally reflect changes of ongoing neural activity that become apparent as synchronized activity in the EEG. To be clear, our results do not suggest that theta power does not contribute to changes in the ERN component. Indeed, we found that all aspects of the theta-band response (i.e., phase coherence, total power, evoked power) modulate with ERN amplitude (sham condition results are shown in Fig. 1*D* and Fig. S1). However, our findings also show that there is at least some aspect of the ERN amplitude that depends on the underlying phase coherence of theta rhythms, such that a selective modification to theta phase dynamics can cause a corresponding modification of the ERN amplitude (anodal condition results are shown in Fig. 1*F* and Fig. S1). Despite the richness of information obtained by combining electrophysiology with a casual neuroscience technique, there remain several nontrivial ambiguities associated with distinguishing between the classical and synchronized oscillation models of ERP generation (41, 42).

1. First MB, Spitzer RL, Gibbon M, Williams JBW (1995) *Structured Clinical Interview for DSM-IV Axis I Disorders* (Biometrics Research Department, New York State Psychiatric Institute).
2. Overall JE, Gorham DR (1962) The brief psychiatric rating scale. *Psychol Rep* 10:799–812.
3. Andreasen NC (1984) *The Scale for the Assessment of Positive Symptoms (SAPS)* (University of Iowa, Iowa City, IA).
4. Andreasen NC (1983) *The Scale for the Assessment of Negative Symptoms (SANS)* (University of Iowa, Iowa City, IA).
5. Reinhart RMG, Woodman GF (2014) Causal control of medial-frontal cortex governs electrophysiological and behavioral indices of performance monitoring and learning. *J Neurosci* 34(12):4214–4227.
6. Reinhart RMG, Carlisle NB, Kang MS, Woodman GF (2012) Event-related potentials elicited by errors during the stop-signal task. II: Human effector-specific error responses. *J Neurophysiol* 107(10):2794–2807.
7. Logan GD, Cowan WB, Davis KA (1984) On the ability to inhibit simple and choice reaction time responses: A model and a method. *J Exp Psychol Hum Percept Perform* 10(2):276–291.
8. Monte-Silva K, et al. (2013) Induction of late LTP-like plasticity in the human motor cortex by repeated non-invasive brain stimulation. *Brain Stimulat* 6(3):424–432.
9. Poreisz C, Boros K, Antal A, Paulus W (2007) Safety aspects of transcranial direct current stimulation concerning healthy subjects and patients. *Brain Res Bull* 72(4-6):208–214.
10. Gandiga PC, Hummel FC, Cohen LG (2006) Transcranial DC stimulation (tDCS): A tool for double-blind sham-controlled clinical studies in brain stimulation. *Clin Neurophysiol* 117(4):845–850.
11. Nunez PL, Srinivasan R (2006) *Electric Fields of the Brain: The Neurophysics of EEG* (Oxford Univ Press, Oxford), 2nd Ed.
12. Woodman GF, Luck SJ (2003) Serial deployment of attention during visual search. *J Exp Psychol Hum Percept Perform* 29(1):121–138.
13. Nelson MJ, Boucher L, Logan GD, Palmeri TJ, Schall JD (2010) Nonindependent and nonstationary response times in stopping and stepping saccade tasks. *Atten Percept Psychophys* 72(7):1913–1929.
14. Kayser J, Tenke CE (2006) Principal components analysis of Laplacian waveforms as a generic method for identifying ERP generator patterns: II. Adequacy of low-density estimates. *Clin Neurophysiol* 117(2):369–380.
15. Srinivasan R, Winter WR, Ding J, Nunez PL (2007) EEG and MEG coherence: Measures of functional connectivity at distinct spatial scales of neocortical dynamics. *J Neurosci Methods* 166(1):41–52.
16. Cavanagh JF, Cohen MX, Allen JJ (2009) Prelude to and resolution of an error: EEG phase synchrony reveals cognitive control dynamics during action monitoring. *J Neurosci* 29(1):98–105.
17. van Driel J, Ridderinkhof KR, Cohen MX (2012) Not all errors are alike: Theta and alpha EEG dynamics relate to differences in error-processing dynamics. *J Neurosci* 32(47):16795–16806.
18. Oostenveld R, Fries P, Maris E, Schoffelen JM (2011) FieldTrip: Open source software for advanced analysis of MEG, EEG, and invasive electrophysiological data. *Comput Intell Neurosci* 2011:156869.
19. Lachaux JP, Rodriguez E, Martinerie J, Varela FJ (1999) Measuring phase synchrony in brain signals. *Hum Brain Mapp* 8(4):194–208.
20. Sadleir RJ, Vannorsdall TD, Schretlen DJ, Gordon B (2010) Transcranial direct current stimulation (tDCS) in a realistic head model. *Neuroimage* 51(4):1310–1318.
21. Fuchs M, Drenckhahn R, Wischmann HA, Wagner M (1998) An improved boundary element method for realistic volume-conductor modeling. *IEEE Trans Biomed Eng* 45(8):980–997.
22. Dale AM, Sereno MI (1993) Improved localization of cortical activity by combining EEG and MEG with MRI cortical surface reconstruction: A linear approach. *J Cogn Neurosci* 5(2):162–176.
23. Pascual-Marqui RD (2002) Standardized low-resolution brain electromagnetic tomography (sLORETA): Technical details. *Methods Find Exp Clin Pharmacol* 24(Suppl D):5–12.
24. Wagner M, Fuchs M, Kastner J (2007) SWARM: sLORETA-weighted accurate minimum norm inverse solutions. *Int Congr Ser* 1300:185–188.
25. Narayanan NS, Cavanagh JF, Frank MJ, Laubach M (2013) Common medial frontal mechanisms of adaptive control in humans and rodents. *Nat Neurosci* 16(12):1888–1895.
26. Gehring WJ, Liu Y, Orr JM, Carp J (2012) The error-related negativity (ERN/Ne). *Oxford Handbook of Event-Related Potential Components*, eds Luck SJ, Kappenman E (Oxford Univ Press, New York), pp 231–291.
27. Jennings JR, Wood CC (1976) Letter: The epsilon-adjustment procedure for repeated-measures analyses of variance. *Psychophysiology* 13(3):277–278.
28. Nichols TE, Holmes AP (2002) Nonparametric permutation tests for functional neuroimaging: A primer with examples. *Hum Brain Mapp* 15(1):1–25.
29. Maris E, Oostenveld R (2007) Nonparametric statistical testing of EEG- and MEG-data. *J Neurosci Methods* 164(1):177–190.
30. Dolan RJ, et al. (1995) Dopaminergic modulation of impaired cognitive activation in the anterior cingulate cortex in schizophrenia. *Nature* 378(6553):180–182.
31. Sanders GS, Gallup GG, Heinsen H, Hof PR, Schmitz C (2002) Cognitive deficits, schizophrenia, and the anterior cingulate cortex. *Trends Cogn Sci* 6(5):190–192.
32. Luck SJ (2005) *An Introduction to the Event-Related Potential Technique* (MIT Press, Cambridge, MA).
33. Goff WR, Allison T, Vaughan HG (1978) The functional neuroanatomy of event-related potentials. *Event Related Brain Potentials in Man*, eds Callaway E, Tueting P, Koslow S (Academic, New York), pp 1–92.
34. Vaughan HG, Jr (1969) The relationship of brain activity to scalp recordings of event-related potentials. Average Evoked Potentials: Methods, Results and Evaluations, ed Lindsley DB (US Government Printing Office, Washington, DC), pp 45–75.
35. Coles MGH, Rugg MD (1995) Event-related potentials: An introduction. *Electrophysiology of Mind*, eds Rugg MD, Coles MGH (Oxford Univ Press, New York), pp 1–26.
36. Basar E (1980) *EEG Brain Dynamics: Relation Between EEG and Brain Evoked Potentials* (Elsevier, Amsterdam).
37. Sayers BM, Beagley HA, Henshall WR (1974) The mechanism of auditory evoked EEG responses. *Nature* 247(5441):481–483.
38. Makeig S, et al. (2002) Dynamic brain sources of visual evoked responses. *Science* 295(5555):690–694.
39. Luu P, Tucker DM, Makeig S (2004) Frontal midline theta and the error-related negativity: Neurophysiological mechanisms of action regulation. *Clin Neurophysiol* 115(8):1821–1835.
40. Luu P, Tucker DM (2001) Regulating action: Alternating activation of midline frontal and motor cortical networks. *Clin Neurophysiol* 112(7):1295–1306.
41. Yeung N, Bogacz R, Holroyd CB, Cohen JD (2004) Detection of synchronized oscillations in the electroencephalogram: An evaluation of methods. *Psychophysiology* 41(6):822–832.
42. Yeung N, Bogacz R, Holroyd CB, Nieuwenhuis S, Cohen JD (2007) Theta phase resetting and the error-related negativity. *Psychophysiology* 44(1):39–49.
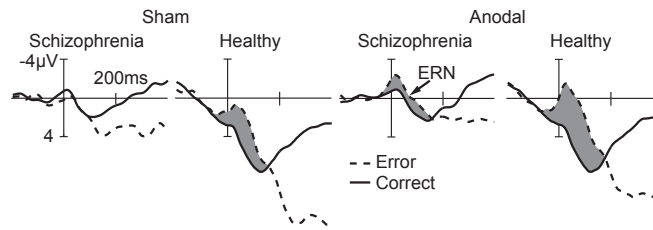
Fig. S1. ERN results. Response-locked grand average ERPs from correct (solid line) and error (dashed line) trials shown at Cz across tDCS conditions and subject groups. The gray-shaded regions show the latency window of the ERN.

Table S1. Demographic Information

Variable	Patients, mean (SD)	Controls, mean (SD)	Statistical test	P value
Age, y	43.1 (7.76)	38.2 (10.78)	$t = 1.59$	0.12
Gender, n			$\chi^2 = 0.003$	0.96
Female	8	8		
Male	11	10		
Duration of illness, y	22.6 (7.86)			
SAPS, total	16.8 (15.37)			
Hallucinations	1.8 (1.75)			
Bizarre behavior	0.7 (1.10)			
Delusions	0.9 (1.22)			
Positive formal TD	0.8 (1.51)			
SANS, total	31.7 (16.92)			
Affective flattening	1.9 (1.49)			
Alogia	1.0 (1.20)			
Avolition apathy	2.8 (0.96)			
Anhedonia asociality	1.9 (1.47)			
Attention	0.8 (0.96)			
BPRS	18.6 (10.60)			
Chlorpromazine dose equivalent	425.05 (250.73) mg·d^{-1}			

The χ^2 value results from a Pearson's χ^2 test. The t value results from an independent two-tailed t test. BPRS, Brief Psychiatric Rating Scale (2); SANS, Scale for the Assessment of Negative Symptoms (4); SAPS, Scale for the Assessment of Positive Symptoms (3); TD, thought disorder.